Effects of liquid turbulent boundary layer spanwise organisation on air lubrication

Laskari, Angeliki

DOI
10.1016/j.ijmultiphaseflow.2025.105383

Publication date
2025

Document Version
Final published version

Published in
International Journal of Multiphase Flow

Citation (APA)
Laskari, A. (2025). Effects of liquid turbulent boundary layer spanwise organisation on air lubrication. *International Journal of Multiphase Flow*, *193*, Article 105383. https://doi.org/10.1016/j.ijmultiphaseflow.2025.105383

International Journal of Multiphase Flow 193 (2025) 105383

Contents lists available at ScienceDirect

International Journal of Multiphase Flow

journal homepage: www.elsevier.com/locate/ijmulflow

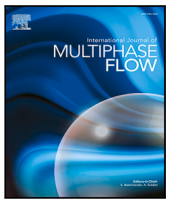

Research Paper

Effects of liquid turbulent boundary layer spanwise organisation on air lubrication

Angeliki Laskari

Process & Energy (Faculty of Mechanical Engineering, Delft University of Technology), Leeghwaterstraat 21, Delft, 2628CB, The Netherlands

ARTICLE INFO

Keywords:
Turbulent boundary layers
Air lubrication
Spanwise meandering
Coherent structures

ABSTRACT

The effect of the streamwise velocity structuring on air lubrication is experimentally assessed in a flat plate turbulent boundary layer. High-speed, planar particle image velocimetry is performed on a wall-parallel plane within the logarithmic region upstream of the air injection, concurrently with high-speed shadowgraphy of the air phase immediately downstream of it. Three different air phase regimes are evaluated (bubbly, transitional, air layer), all deeply embedded in the log region and for a constant liquid freestream velocity. Air bubbles formed downstream of low-speed streaks are found to be larger and to convect much slower than those formed downstream of high-speed events. The spanwise variation of air coverage and its time evolution follow the spanwise structuring and evolution of log-region residing streaks for both the bubbly and transitional regimes, with low-speed streaks promoting air coverage and high-speed ones inhibiting it, a correlation stronger closer to the injector but remaining significant for large downstream distances ($x > 4\delta$). High-speed streaks are also shown to be largely responsible for liquid pockets developing close to the injector in the air layer regime, locally breaking its spanwise continuity.

1. Introduction

The current focus on urgent climate actions and the resulting goals and mandatory measures for many industries has brought a lot of attention in developing appropriate and scalable technologies that can achieve fast decarbonisation. For the maritime industry, this has meant interest for a diverse array of approaches, ranging from alternative fuels and super-hydrophobic coatings, to electric propulsion, renewable energy sources on board, and related energy regeneration strategies. From a hydrodynamics perspective, there has been intense focus in understanding and harnessing the capacity of air injection for turbulent drag reduction in liquid flows (see Ceccio, 2010; Murai, 2014, for reviews), promising significant reduction in ship resistance and thus emissions. The increasing use of such technologies in seagoing vessels highlights the extent of their potential (see Silberschmidt et al., 2016; Kim and Steen, 2023), however scalability remains an open issue, necessitating further research. From a fundamental physics standpoint, the different mechanisms responsible for drag reduction are still debated (Murai, 2014; Winkel et al., 2004; Verschoof et al., 2016; Lo et al., 2006; Spandan et al., 2017), and full-scale predictions, of particular interest to the industry, remain elusive.

Early experimental and numerical studies on air lubrication have mostly focused on micro-bubble injection, which was shown to have important drag reduction capabilities, especially when bubbles were contained within the buffer sublayer (McCormick and Bhattacharyya, 1973; Madavan et al., 1985; Deutsch and Castano, 1986; Gabillet et al., 2002; Latorre et al., 2009; Ferrante and Elghobashi, 2004; Harleman et al., 2011, among many others). However, such sub-millimetre sized bubbles are also bound to migrate away from the wall due to bubble lift forces, leading to significant losses in performance especially in large-scale setups (Sanders et al., 2006; Tanaka et al., 2022). Thus, more recent studies on the topic have shifted their interest from sub-millimetre bubble injection to larger bubbles and air layers (produced by an increase in the air injection rate Q_{air}). The effectiveness of drag reduction in such systems depends heavily on bubble size and coalescence behaviour with increasing Q_{air}: deformability of large bubbles is a key drag reduction mechanism in bubbly flows (Lu et al., 2005; van den Berg et al., 2005; Elbing et al., 2008; Park et al., 2019), while a stable air layer formation due to bubble coalescence leads to the largest possible drag reduction in a flat plate turbulent boundary layer (TBL) (Elbing et al., 2008). These air phase characteristics heavily rely, in turn, on the turbulent liquid phase, and the presence of turbulence.

From a fundamental flow physics viewpoint, dependence of bubble deformation and breakup on liquid turbulence (homogeneous and isotropic) was already established by 1955 (Hinze-Kolmogorov hypothesis, Kolmogorov (1949), Hinze (1955)). Various investigations exploiting this framework have since overwhelmingly focused on small-scale turbulence effects on bubbles/droplets in homogeneous isotropic

E-mail address: A.Laskari@tudelft.nl.

https://doi.org/10.1016/j.ijmultiphaseflow.2025.105383
Received 30 January 2025; Received in revised form 6 June 2025; Accepted 28 July 2025
Available online 6 August 2025

flows (Masuk et al., 2021), but also dispersed in turbulent jets (Ravelet et al., 2011), or in breaking waves (Deike, 2022). While several studies on the topic have also expanded to include effects of large-scale shear forcing in configurations more similar to air lubrication (homogeneous shear (Rosti et al., 2021) and Taylor–Couette flows (Spandan et al., 2016)), a large majority of neutrally buoyant droplets or positively buoyant bubbles in such cases will move away from solid boundaries and get dispersed in the flow. In air lubrication however, buoyancy will keep large bubbles and air pockets entirely bound to the high shear region of the liquid TBL, with only a thin layer of liquid separating them from the solid wall and allowing them to slide (Park et al., 2019).

Effects of the liquid flow on such air lubrication configurations (and thus on characteristics and drag reduction of wall-sliding bubbles and air pockets) have been explored in more applied studies; however, most have either overlooked turbulence effects or have been scale limited, or both. In typical cargo ships, the boundary layer thickness is expected to reach $\delta \simeq \mathcal{O}$(m) and ratios of $t_{air}/\delta \ll 1$ are relevant (where t_{air} is the thickness of the air phase). Investigations of large, deformable bubbles with a small t_{air}/δ ratio thus require correspondingly large facilities. Turbulent fluctuations can then no longer be ignored and include significantly more complex considerations due to the temporal and spatial variations of velocity and shear in the vicinity of the air phase. These become increasingly critical for air lubrication systems which do not make use of backwards facing steps (cavitators) upstream of the air injection. Such systems are much simpler and less costly (both in construction and in operation) and thus of particular industrial importance. They will be the focus for the remainder of this section and of our analysis in the sections that follow.

Experimental (Park et al., 2014; Oishi and Murai, 2014) and numerical (Kim et al., 2021) studies of large deformable bubbles immersed on the top half of horizontal (and tilted) turbulent channel flows, assessed the two-way interaction between the air phase and liquid turbulence, with visualisations in wall-parallel planes of bubble effects on vortical structures (Park et al., 2014), as well as resulting skin friction variations (Oishi and Murai, 2014), however these have been limited to $t_{air}/\delta > 0.5$ and $Re_\tau < 300$. In similar configurations, with slightly lower thickness ratios ($t_{air}/\delta \approx 0.3$) (Yoon et al., 2022a,b) have assessed bubble size and velocity distribution with respect to bulk flow velocity (or plate inclination), however turbulence effects were not discussed. On the other end of the spectrum, in a very large scale facility ($Re_\tau > 10^4$) (Elbing et al., 2008) assessed the effect of doubling the incoming boundary layer thickness on the resulting bubble drag reduction and found it to be negligible; however, there was no further discussion on the effect of turbulence on other characteristics of the air bubbles or air layers, since the focus was primarily on drag reduction. More recently, Nikolaidou et al. (2024) highlighted the significant effects of the global upstream characteristics of a turbulent TBL ($0.07\delta \leq t_{air} \leq 0.3\delta$ and $Re_\tau > 3000$), such as δ and U_∞, on both the air phase regime transition and the air layer topology. Additionally, the authors underlined the importance of the local mean velocity in the vicinity of the air layer $U(y = t_{air})$, as opposed to the global freestream velocity, U_∞, indicating the significant effect of the wall-imposed inhomogeneity.

Although there is still much to investigate regarding such *average incoming flow* effects on the entire range of air phase regimes, there is still a completely unexplored area in the context of *instantaneous* structuring of the incoming flow, such as the well established meandering of streamwise velocity fluctuations in the logarithmic region of TBLs (see Hutchins and Marusic, 2007a; Dennis and Nickels, 2011; Kevin et al., 2019, among many others). In a single wall-parallel plane, although the mean streamwise velocity will be constant, instantaneously, quite significant variations are expected, not only in time (streamwise velocity fluctuations are quite elongated in the streamwise direction), but more importantly in the spanwise direction. Their impact on air lubrication configurations, especially for $t_{air}/\delta \ll 1$ remains unknown.

Table 1
Nominal liquid flow conditions | PIV details.

U_∞ [ms^{-1}]	U_τ [ms^{-1}]	δ_{99} [m]	Re_τ [-]	dx^+ [-]	dt^+ [-]	L_x [m]	L_z [m]
0.89	0.034	0.095	3200	13	2.3	4.5δ	2.6δ

Within this context, in the present work, we assess for the first time, effects of the instantaneous, spanwise inhomogeneity of log-region-residing turbulent structures on downstream air injection by simultaneous high-speed measurements of both the liquid and the air phases. The goal is to assess how much of the variation in bubble size and velocity in the bubbly regime (low air flow rates), as well as air coverage in the transitional and air layer regimes (higher air flow rates), are affected by the instantaneous structuring of the incoming flow, for a constant freestream velocity.

In the next sections, the experimental setup and measurement details will be outlined, followed by results on both the liquid and the air phases as well as relevant discussions and conclusions.

2. Experimental setup

In this work, simultaneous high-speed shadowgraphy (SDG) of the air phase and planar Particle Image Velocimetry (PIV) of the liquid phase were performed, in the recirculating water tunnel of the A&H laboratory of the Process and Energy Department. The tunnel has a 5 m long test section with a 0.6 m×0.6 m cross-section, is optically accessible from all sides and operates at freestream speeds of $U_\infty = 0$–1 ms^{-1}. Two transparent plates covering the free surface and spanning the entire width and length of the test section were placed side by side on the tunnel top, allowing the development of a liquid TBL underneath, tripped using a zigzag strip (0.5 mm thickness) at the leading edge of the upstream plate. Air was injected at a streamwise distance of 3.95 m downstream of the strip, through a thin (4 mm) rectangular slot spanning 0.58 m in width. More details on the injection slot configuration and the setup can be found in Anand et al. (2025) and Nikolaidou et al. (2024). In what follows, x (U), y (V), and z (W) will be used to denote the streamwise, wall-normal, and spanwise directions (velocity components), respectively. In the unified coordinate axis system for both PIV and SDG, $(x, z) = (0, 0)$ corresponds to the upstream edge of the injector slot (see also Fig. 1(c)). For the flow velocities, Reynolds decomposition is employed: $U = \overline{U} + u'$, with the overbar denoting a time-average: $\overline{U} = \langle U \rangle_N$, where N is the number of snapshots (see also Table 2 in what follows).

The nominal flow conditions and boundary layer thickness of the single phase liquid TBL flow immediately upstream of the injector were assessed in the same setup by an earlier planar PIV campaign on a streamwise-wall-normal plane (x–y, Nikolaidou et al., 2024): $U_\infty = 0.89$ ms^{-1}, $\delta_{99} = 0.095$ m, $Re_\tau = u_\tau \delta_{99}/\nu = 3200$ (see also Table 1). These will be used for all normalisations in what follows, with $\delta = \delta_{99}$.

Single camera, planar low- and high-speed PIV was performed on a x–z plane, at a wall-normal distance of $y = 10 \pm 0.5$ mm ($\sim 0.1\delta$). The PIV plane was specifically chosen to coincide with the maximum expected thickness of the air phase, based on air layer regime estimates in Nikolaidou et al. (2024). Due to our interest in large-scale meandering velocity structures in the log region, the effect of the uncertainty associated with the measurement plane location is considered to be negligible on the results presented here. This wall-normal location was kept constant for all air phase regimes tested and was the same as that of the focal plane of the shadowgraphy camera (see also next paragraph). A Phantom 640-L camera, fitted with a Nikon 105mm Nikkor lens, was used for imaging from the top (see Fig. 1(a)), at a frequency of $f_{acq} = 500$ Hz (resulting in a timestep of $dt^+ = 2.3$, Table 1) for the high-speed datasets (for the low-speed ones this was kept < 0.1Hz). A Litron LDY300 YLF laser beam was guided via a series of mirrors towards the side windows of the test section, expanded through a cylindrical

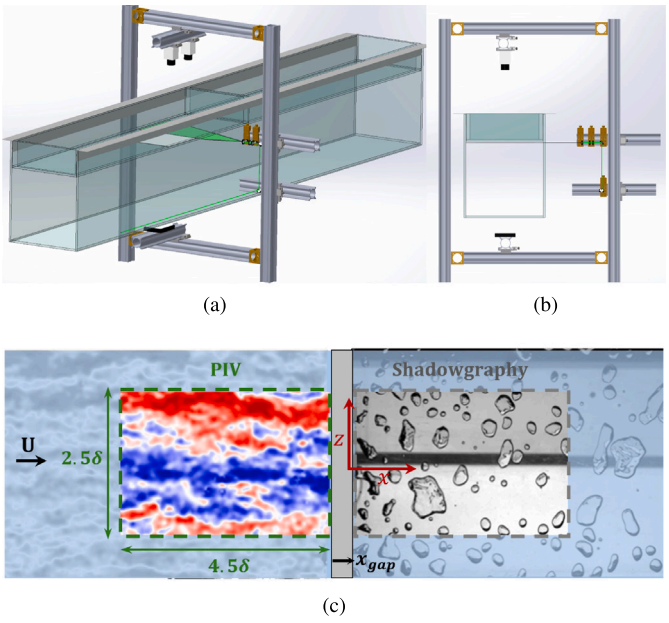

Fig. 1. Illustration of experimental setup in an isometric (a) and side (b) view. The LED illumination is from the bottom, imaging is from the top and the laser light enters the test section from the front. Illustration of measurement domain (c), including the PIV (green) and shadowgraphy (grey) planes. (For interpretation of the references to colour in this figure legend, the reader is referred to the web version of this article.)

and spherical lens, into a thin light sheet (∼1mm), before entering the tunnel to illuminate the targeted wall-parallel plane (expanding in x). Cutting off the downstream expansion of the light sheet just prior to the injector location eliminated any laser/gas interference. The system was synchronised via a LaVision PTU controller, and images were acquired and processed via DaVis 10 software. The imaged field of view (FOV) was $4.5\delta \times 2.6\delta$ in x and z, respectively, with a final interrogation window size of 32 pix × 32 pix (2.5 mm × 2.5 mm) and a 50% overlap (resulting in a vector spacing of $dx^+ = 13$, Table 1) .

Single camera, planar high-speed shadowgraphy (SDG) was performed simultaneously and on the same x–z plane as PIV, but located at a distance $x_{gap} = 0.5\delta$ downstream of it (see also Fig. 1(c) for an instantaneous velocity field of the liquid phase together with the imaging of the air phase), with the same camera and lens combination, ensuring the same magnification and FOV as the PIV, while simultaneous calibration allowed accurate spanwise alignment. The streamwise gap between the PIV and shadowgraphy FOVs, x_{gap}, was necessitated due to the non-transparent material used for the injector (see Fig. 1(c)). For correlations between liquid and gas characteristics, PIV and shadowgraphy images were then matched using the global mean velocity of the incoming TBL and inferring Taylor's Hypothesis; the use of a local mean was also tested, however it did not significantly alter the results presented here. Illumination was provided by side-by-side LED panels placed underneath the bottom windows of the water tunnel. Three different air flow rates (Table 2) at the same liquid freestream velocity, U_∞, were tested, corresponding to three distinct air phase regimes (bubbly, transitional, and air layer, see also Fig. 2) such that the effect of the incoming TBL organisation on each one of them could be separately assessed. For more details on the regime classification and topology, the reader is referred to the work by Nikolaidou et al. (2024). As mentioned above, the same x–z plane as the PIV ($y = 0.1\delta$) was chosen as the focal plane for all air flow rates Q_{air}, and led to sufficient focus of the air phase, indicating an approximately constant thickness of the air bubbles, pockets, and air layers.

In terms of data acquisition, a low-speed PIV dataset of the single phase TBL (Case A - no air present) was acquired first (a set of N_{ls} image-pairs, see also Table 2), in order to allow for a statistical analysis of a baseline case. Subsequently, for each air phase regime (Cases B), a single low-speed PIV dataset as well as multiple concurrent high-speed PIV and SDG datasets were acquired (adding up to N_{hs} images, see also Table 2), to allow for both a statistical analysis of the upstream liquid flow (and potential effects due to the air injection) and a time-resolved analysis of the liquid-air interaction, respectively.

Table 2
Dataset details for all cases. N_{ls} denotes the number of low-speed PIV image-pairs and N_{hs} the total concurrent, high-speed PIV and SDG images in time-resolved sets. Q_{air} is in $lmin^{-1}$.

	Data	Regime	Q_{air}	N_{ls}	N_{hs}
A	PIV	No air	0.0	1303	–
B1	PIV/SDG	Bubbly	10.3	2596	22 × 3059
B2	PIV/SDG	Transitional	15.5	2604	13 × 3059
B3	PIV/SDG	Air Layer	41.2	2602	5 × 3059

3. Results

3.1. Liquid TBL - all cases

Before delving into the air phase characteristics and the level of their dependence on the upstream liquid flow, it is necessary to first examine the liquid TBL itself, with and without the presence of air. It should be noted that all normalisations in what follows are with respect to the global single phase (liquid) TBL quantities immediately upstream of the air injector ($x = 0$, see Table 1). Further, all velocities are normalised with outer variables (without additional notation for readability), unless otherwise noted.

The first thing to note when examining $\overline{U}$ of the liquid TBL (Case A, see Fig. 3(b)), is that a clear mean spanwise inhomogeneity exists (reaching a maximum of 30%), not expected given the canonicality of the flow geometry; u' and v' exhibit similar behaviour (with decreased activity in regions where $\overline{U}$ is low), while the spanwise mean velocity is mostly unaffected. We will return to this behaviour in the following paragraphs. The effect of air on both the magnitude and spatial coherence of the upstream mean and fluctuating liquid velocity is marginal, with a mean deceleration close to the injector being the most prominent, due to air-induced blockage (see also discussion in Nikolaidou et al., 2024). In terms of spatial coherence for both fluctuating velocity components (see Figs. 3(c) and 3(d)), there is an overall agreement with previous canonical TBL studies (Kevin et al., 2019; Tutkun et al., 2009; De Silva et al., 2018, among many others). The slight increase of u' with x in the baseline case (Fig. 3(b)) can be attributed to the development of the TBL and the global normalisation applied (≈10% increase in δ and ≈1% decrease in U_τ is expected within the FOV). This effect is amplified in the region close to the injector when air is present (Cases B1-3), proportionally to an increase in Q_{air}, due to the adverse pressure gradient effects imposed by the air-induced blockage, which becomes stronger and more homogeneous in the spanwise direction as Q_{air} increases (see Fig. 2). However, these deviations are expected to be negligible at distances $x < -2\delta$ (injector located at $x = 0$). Instantaneously (and even closer to the injector than our setup allows), the liquid TBL might exhibit stronger effects due to the gas presence, however this side of their two-way interaction is in any case out of scope of the present study; our focus rests solely on the effects of the TBL on the injected air instead. Evidently, targeting the region immediately upstream and downstream of the injector would illustrate any interactions more clearly, however our goal is to provide a general and robust framework of the large-scale TBL effects on the air topology downstream, for which the current database and following analysis are sufficiently suitable.

Returning to the streamwise mean flow inhomogeneity, present in all examined cases, it came to light only after assessing the flow

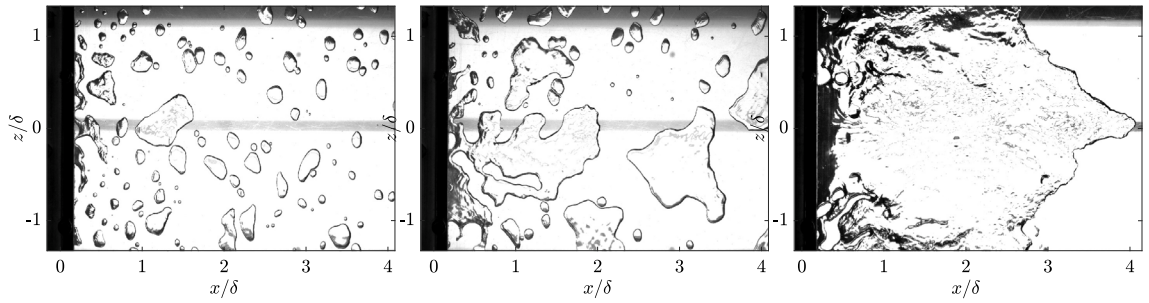

Fig. 2. Shadowgraphy images for the three Q_{air} tested, each corresponding to a different air phase regime: (a) bubbly (Q_{air} = 10.3 lmin^{-1}), (b) transitional (Q_{air} = 15.5 lmin^{-1}), and (c) air layer regime (Q_{air} = 41.2 lmin^{-1}). Flow is from left to right.

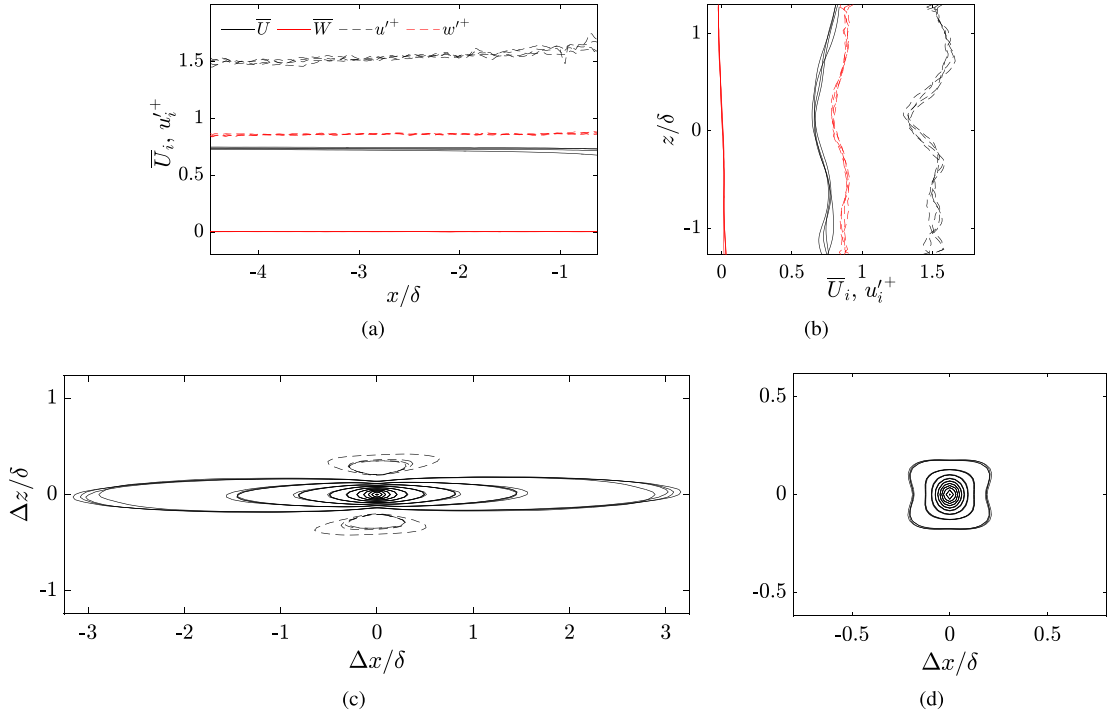

Fig. 3. Liquid TBL (All Cases) - x (a) and z (b) variation of mean velocities and turbulence intensities, two point correlations of u' (c) and w' (d). Mean velocities and rms fluctuations are outer- and inner-normalised, respectively. Contour levels from −0.1 to 1 with a spacing of 0.1 (dashed lines indicating $R_{uu} < 0$).

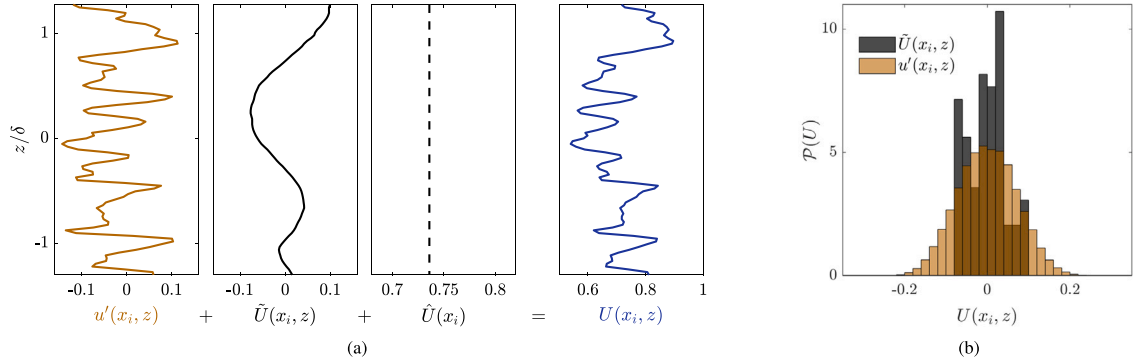

Fig. 4. Liquid TBL (Case A) - (a) An instantaneous example of the spanwise variation of U at $x_i = -2.5\delta$ (blue) as decomposed into a fluctuating turbulent component (u', yellow), a spanwise varying ($\tilde{U}$, solid black) and a spanwise constant mean ($\hat{U}$, dashed black line). (b) Probability density functions (p.d.fs.) of the fluctuating turbulent and mean components in all captured snapshots, N_{ls}. All velocities are outer-normalised. (For interpretation of the references to colour in this figure legend, the reader is referred to the web version of this article.)

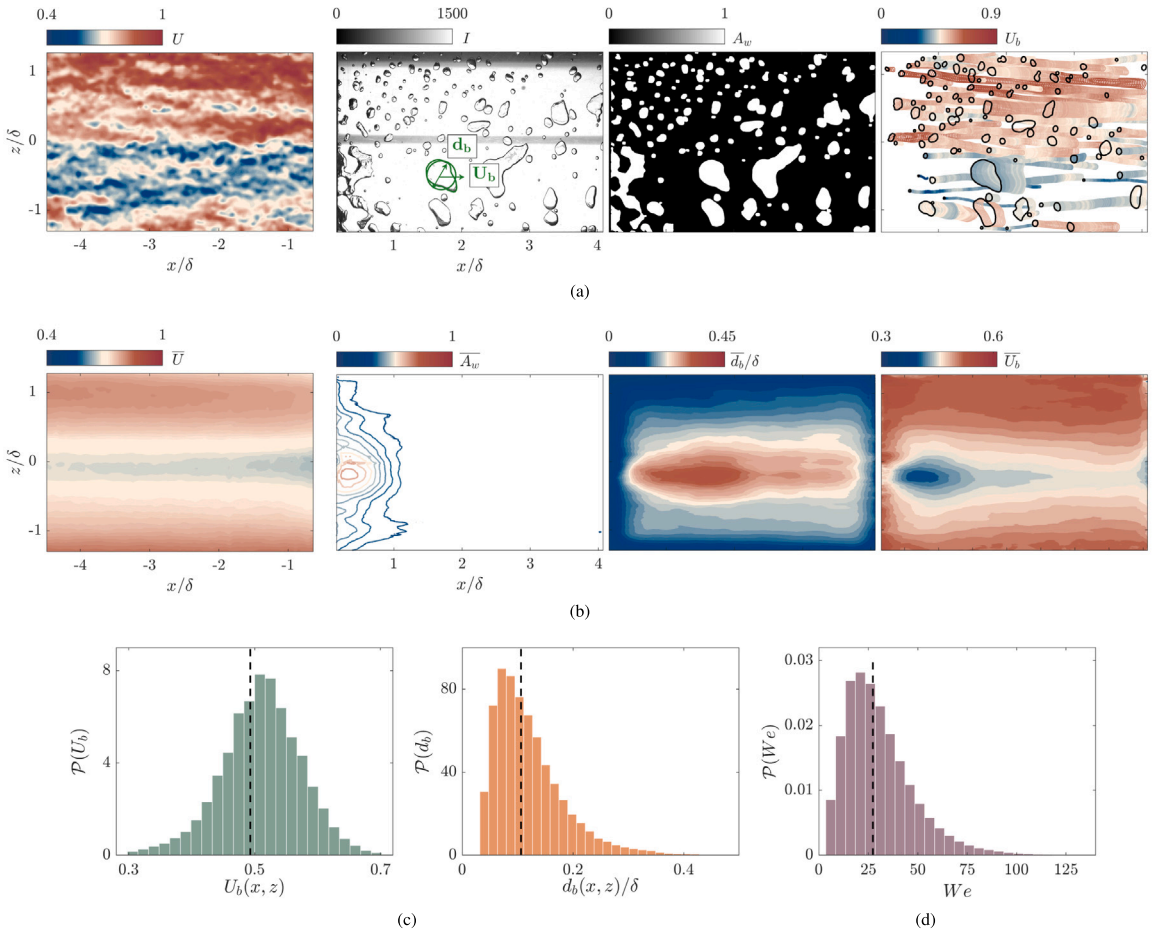

Fig. 5. Liquid TBL and bubbly regime (Case B1) - (a) Instantaneous liquid velocity (left), air phase (equivalent bubble diameter, d_b, and velocity U_b, schematically shown in green), corresponding wall-projected area A_w, and identified bubble tracks, coloured according to the instantaneous bubble streamwise velocity, U_b. (b) Mean liquid velocity (left), $\overline{U}$, wall-projected area, $\overline{A_w}$, equivalent bubble diameter, $\overline{d_b}$, and bubble velocity, $\overline{U_b}$, for all datasets. Flow is from left to right. (c) Probability density functions of U_b and d_b and the corresponding global averages, denoted with dashed lines. (d) Corresponding Weber number, $We = (\rho U_b^2 d_b)/\gamma$. All velocities are outer-normalised. (For interpretation of the references to colour in this figure legend, the reader is referred to the web version of this article.)

characteristics in a spanwise plane, and the main reason behind it is assumed to be the formation of the TBL on the ceiling of the water tunnel. The consequence of such a setup is that a 'clean' start of the TBL at the trip location is not possible (the TBL starts developing within the water tunnel contraction), so any potential misalignment in any of the ceiling covers will disturb downstream evolution. While this is certainly not ideal, we can still move forward in exploring the effect of the instantaneous liquid flow organisation on the air phase, albeit with care. We will take heed of this mean deviation from canonical behaviour in our analysis: in canonical cases, the mean is constant in z and only the fluctuations' spanwise inhomogeneity can have an effect on the air behaviour, while here the influence of the fluctuations will be compounded with that of the mean flow. As such, their effects will be separately assessed, wherever possible.

Within this context, to establish the relative importance of these two sources of inhomogeneity, we consider their spanwise variation in a single streamwise location ($x = -2.5\delta$) such that any potential boundary layer development effects are removed (different streamwise positions and cases were also tested, with the same observed behaviour). Following the Reynolds decomposition of the velocity discussed earlier, we further decompose the mean velocity component into a spanwise constant mean $\hat{U}$, and a spanwise varying mean $\tilde{U}(z)$, such that: $U = \overline{U} + u' = \hat{U} + \tilde{U} + u'$; in a canonical TBL, the second term of the right hand side is zero, while in our case it varies along z (black solid line in Fig. 4(a)) with an amplitude comparable (and slightly lower) to that of the fluctuating turbulent component (see probability density distributions in Fig. 4(b)). There are two main things to note regarding these results. On one hand, the magnitude of instantaneous fluctuations is significant: it can reach up to ±15% of the freestream at this wall-normal location. This means that the gas injected within spanwise alternating high- and low-speed streaks can experience spanwise velocity differences (peak-to-trough) of up to 30% of U_∞. In the absence of a mean variation, this will also be the only possible source of any liquid-induced gas spanwise inhomogeneity observed. On the other hand, the spanwise variation of the mean in our case is of the same order as the fluctuations (albeit with less extreme excursions) and it is thus also expected to play an important role. In terms of spatial scales, the two-point correlations of turbulent fluctuations indicate an average spanwise extent of $\approx 0.2\delta$, while the fluctuations of the mean extend more than twice that distance, a difference which should also be taken into account when attempting to distinguish their respective effects on the air phase.

In what follows, the three air phase regimes (bubbly-B1, transitional-B2, air layer-B3) will be assessed in conjunction with the upstream liquid flow and in particular its instantaneous large-scale spanwise inhomogeneity and time evolution.

3.2. Air phase

3.2.1. Bubbly regime — case B1

We start the air phase analysis with the bubbly regime (Case B1), in which the air forms individual bubbles (see Fig. 5(a), for an instantaneous example and supplementary video S1). It has been well

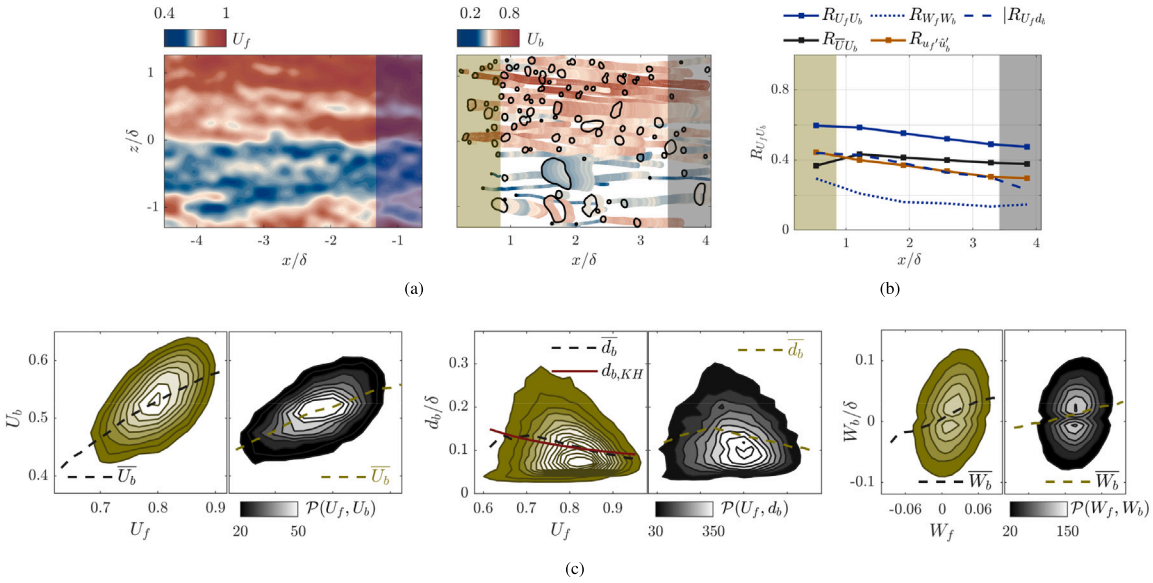

Fig. 6. Liquid TBL and bubbly regime (Case B1) - (a) Filtered TBL velocities, U_f (left) at the downstream end of the PIV FOV (shaded in blue) are correlated with U_b, W_b, and d_b of bubbles (right) in regions of the same extent but centred at different streamwise locations of the SDG FOV (examples shaded in light green and grey). Flow is from left to right. (b) Resulting correlation coefficients for these regions along x. (c) Representative joint p.d.fs. for these correlations, for bubbles at the most upstream (light green) and downstream (grey) locations in (a) (colourbars apply to both). Joint p.d.fs. are normalised with the total volume such that $\iint \mathcal{P}(X,Y) = 1$. Solid red line in the middle panel indicates d_b based on Eq. (1) and assuming a linear decrease in U_τ with U_f. (For interpretation of the references to colour in this figure legend, the reader is referred to the web version of this article.)

established that an increase in U_∞ (and thus U_τ) leads to the formation of smaller bubbles (Hinze, 1955), which also move faster (at approximately half the speed of the surrounding liquid (Tanaka et al., 2020)). The goal of the present analysis is then to assess the extent to which the spatial and temporal variations of the liquid velocity within the TBL itself can lead to local variations of characteristics of bubbles injected downstream, especially given the fact that there is no backwards facing step (cavitator) present: the air is injected directly in the spatially developing TBL. Due to the injector geometry (spanwise slot without the use of porous plates) and the liquid freestream velocity ($U_\infty = 0.89\text{ms}^{-1}$), the resulting bubbles, bound to the high shear region near the plate due to buoyancy, are large ($\overline{d_b^+} = 320$, see Fig. 5(c) and discussion in Lu et al., 2005) and generally non-spherical (middle panel in Fig. 5(a)). With $We_t = (\rho U_b^2 d_b)/\gamma > 1$ (ρ and γ the liquid density and surface tension, respectively, see Fig. 5(d)), they can also be considered deformable (Spandan et al., 2018). The range of scales present in the liquid TBL and the possible bubble-bubble interactions together with the significant bubble deformability and polydispersity make theoretical predictions for their kinematics quite challenging (Magnaudet and Eames, 2000). We will touch upon the topic from an experimental perspective, however our goal here is not to explicitly describe those kinematics, but rather to assess their level of dependence on the incoming flow.

To this end, we focus on the effects of the incoming flow on three distinct characteristics of the air phase: the total wall-projected area covered by bubbles, A_w, the individual equivalent diameter of the bubbles, $d_b = \sqrt{4A_b/\pi}$ (where A_b is the wall projected area of each bubble), and their velocity $\mathbf{U_b} = (U_b, W_b)$ (see Fig. 5(a)), the latter two via an in-house algorithm tracking the displacement of bubbles' centres (based on A_b). The algorithm excludes splitting or merging events (by imposing area variation limits at each time step) and bubbles located at all domain edges (due to the inherent bias in their characteristics). Given also the need of accurate tracking, bubbles which can be tracked for less than 10 consecutive snapshots are also excluded, leading to a total of ≈ 48000 tracks, with an average track length of 100 snapshots ($t = 0.2s$), thus ensuring sufficient data for convergence of both bubble geometry and bubble velocity statistics. For short tracks ($t < 0.1s$), velocities are considered constant and estimated via linear interpolation of each track (with $1 - R^2 < \mathcal{O}(10^{-5})$), while for the rest, local gradients based on a central difference scheme are used. In contrast to individual bubble characteristics, the total wall-projected area estimate (A_w) does not exclude any bubbles, since the focus is on the instantaneous non-wetted area topology, and not on individual bubble motion; this further ensures that potential loss of information in d_b with respect to air coverage due to these exclusions, is still captured in A_w. The main difference between the two is the inclusion of larger gas pockets in A_w, mostly still attached to the injector, as well as any bubbles at the edge of the domain (see also Fig. 5(a)). Air pockets attached to the injector can be identified by their highly non-spherical shape, a size much larger than a typical bubble and often even including liquid pockets within, and with a large extent of their upstream edge remaining connected to the most upstream location of the FOV over time (see also supplementary video S1).

At a first level, we assess the spatial maps of the average bubble characteristics, in conjunction with the average streamwise velocity of the liquid phase (see Fig. 5(b)). It is immediately apparent that the *spanwise* variation of the latter dictates to a large extent the average diameter and streamwise velocity of the bubbles downstream, throughout the streamwise extent of the FOV ($L_x = 4.5\delta$). Bubbles formed in the spanwise region where the upstream liquid mean flow is slower ($\tilde{U} < 0$, see also Fig. 4(b)) are also slower and larger than the global averages (Fig. 5(c)), while the opposite is true for bubbles downstream of regions with a higher liquid mean flow (correlations of $R_{\overline{UU_b}} = 0.83$ and $R_{\overline{Ud_b}} = -0.76$, respectively). The causal relationship here follows from the fact that the mean liquid flow already exhibits the same spanwise variation without air being present (see also Fig. 3(b)) and thus it imposes a similar effect on the air phase when air is injected. With regards to the *streamwise* variation, $\overline{U}$ exhibits a deceleration close to the injector, consistent with the adverse pressure gradient effect due to the air blockage. The bubble characteristics on the other hand reveal a slightly more homogeneous behaviour in z as the distance from the injector increases, with a return to a smaller d_b and larger U_b in the mid-span, indicating a decrease in sensitivity on the upstream TBL conditions. However, the mid-span is also the location where larger, more deformable bubbles are present, which create a distinct inhomogeneity in air coverage and are expected to create stronger

intra-bubble effects. As such they might also contribute to this observed variation in the spatial averages. Finally, in terms of global statistics, the estimated average bubble speed ($\overline{U_b} = 0.5U_\infty$) agrees well with that measured experimentally in air-lubricated towed models (Tanaka et al., 2020) and the average bubble diameter ($\overline{d_b} = 0.1\delta$) is comparable to the maximum predicted by the Kolmogorov-Hinze theory (KH), as adapted for a TBL by Sanders et al. (2006) ($d_{b,max} = 0.11\delta$, see also Eq. (1), where $\kappa = 0.41$ is the von-Karman constant and $y_b = 0.05\delta$ the approximate distance of the bubbles' centres from the wall). In that study, flat-plate air lubrication by bubbles was experimentally assessed and a similar agreement between the measured average bubble diameter and theoretically predicted maximum was observed.

$$d_{b,max} \approx \left(\frac{\gamma}{2\rho}\right)^{3/5}\left(\frac{\kappa y_b}{U_\tau^3}\right)^{2/5}. \tag{1}$$

Returning to our results, a significant spread exists around both $\overline{U_b}$ and $\overline{d_b}$ (Fig. 5(c)), which is, as discussed above, at least partly due to the spanwise variation of $\overline{U}$. In what follows, we will also assess the level of influence that the *instantaneous* U variation has on these bubble characteristics and on their time evolution. In order to do that, the instantaneous U fields are first filtered with a 2D Gaussian kernel ($\sigma = 2$) of a size equal to the length and width of the u' two-point correlation at $R_{u'u'} = 0.25$ (Fig. 3(c)), following the procedure used in Kevin et al. (2019) for assessing the meandering behaviour of log-region velocity streaks. Correspondingly, the W fields are filtered with a kernel of size equal to the extents of $R_{w'w'} = 0.25$ (Fig. 3(d)). In this way, we can focus on the effect of the large-scale velocity organisation of the filtered fields (U_f, see Fig. 6(a), left) on the air phase, and remove any small-scale influences. Filtering has also been shown to facilitate the reconstruction of long velocity structures in larger downstream distances, when Taylor's hypothesis is used (Dennis and Nickels, 2008). As mentioned in the previous section, the latter is employed (using the global mean liquid velocity as the convection velocity) in order to synchronise the two phases, due to the streamwise distance of the two FOVs: a region of interest within a PIV snapshot taken at time t will be correlated with a region of interest within a SDG snapshot at time $t + (x_{lg}/\overline{U}f_{acq})$, where x_{lg} is the streamwise distance between the two regions (including x_{gap}, see also Section 2). For all air injection cases (Cases B), we focus on the most downstream end of the PIV fields, due to its proximity to the air phase; for the latter, various distances downstream of the injector are examined, depending on the gas characteristics of interest.

We first assess the average correlation between U_f at a region immediately upstream of the injector, and U_b, W_b, and d_b, at regions of equal length but centred at various streamwise locations downstream of the injector (see shaded regions in Figs. 6(a) and 6(b)). The streamwise extent of the regions, $l_x = 0.67\delta$, was chosen for consistency with the one used for the temporal correlations which follow — more details on that choice can be found in Appendix A. For what concerns the spatial correlations discussed here, the effect of l_x on the results was found to be negligible. Examining the results, it is clear that the streamwise bubble velocities are those more strongly correlated with the instantaneous flow upstream of the injector, with an expected drop in correlation as the distance of the bubble from the injector increases (Figs. 6(b) and 6(c)). Regardless, $R_{U_f U_b} > 0.5$ throughout the FOV extent ($\approx 4.5\delta$), indicating a strong influence of the incoming flow on U_b, regardless of the bubbles' size, location, or the presence of other bubbles. As mentioned previously, the spanwise variation in U is due to both $\overline{U}$ and u'; thus here, we also assess their correlation with U_b and u'_b, respectively, in order to evaluate their importance separately. Streamwise velocities of bubbles close to the injector exhibit similar dependence on the upstream $\overline{U}$ and u' ($R_{\overline{U}U_b} \approx R_{u'u'_b} \approx 0.4$); farther downstream, the correlation of the fluctuating component decreases more rapidly than that of the mean, as expected (Fig. 6(b)). These results, in conjunction with the higher values for $R_{U_f U_b}$, indicate that the instantaneous, incoming flow inhomogeneity in z is strong enough to affect bubble speeds downstream, and, despite the fact that the mean component has an important role in our case, the fluctuating component is equally crucial: the mean inhomogeneity itself is not sufficient to explain the liquid-induced bubble motion downstream. It is then safe to assume that in canonical conditions, velocity fluctuations being the only source of inhomogeneity, would still affect bubble motion in large distances downstream of the injector. With respect to the spanwise velocity component, it is lower in amplitude (Fig. 3(a)) and coherent for much shorter extents than u' (Fig. 3(d)) and thus, as expected, has a much more minor effect on W_b ($R_{W_f W_b} \approx 0.2$), albeit still statistically significant, especially for bubbles close to the injector (see also Fig. 6(c), right).

Finally, significant (anti-)correlation exists between the instantaneous incoming flow velocity and the resulting bubble size: bubbles injected downstream of high speed streaks are expected to be smaller, while larger ones would be more often found downstream of low-speed streaks, especially close to the injector ($R_{U_f d_b} = -0.4$ in Fig. 6(b)). When examining the joint p.d.f. leading to this correlation (Fig. 6(c), middle panel), it becomes clear that high-speed streaks are associated with a very narrow bubble size distribution and a low average ($\overline{d_b} = 0.08 \pm 0.03\delta$), while a much wider bubble size range is achievable downstream of low-speed streaks but distributed around an almost twice as large average ($\overline{d_b} = 0.14 \pm 0.08\delta$). This last result is indicative of a more general anti-correlation between air coverage and high-speed streaks, eventually more crucial in the transitional (Case B2) and air layer (Case B3) regimes. The effect diminishes at large downstream distances, although still retaining a statistically significant correlation ($R_{U_f d_b} = -0.2$). While it is intuitively simple to interpret an increase in U_b when the upstream liquid velocity is increasing, the subsequent reduction in bubble size is a little less so. Looking at the KH prediction of the maximum bubble size in a TBL (Eq. (1)), a large d_b variation in a x–z plane can only be traced back to a variation of U_τ within that plane. It has been well established that U_τ is indeed positively correlated with velocity fluctuations, where positive shear events are associated with high-speed structures and vice-versa (Hutchins et al., 2011; Gomit et al., 2020; Guerrero et al., 2020, among others). Here thus, for a variation of U_f from $0.6U_\infty$ to $0.95U_\infty$, leading to an almost 50% decrease in $\overline{d_b}$, we expect a corresponding increase in U_τ. Alfredsson et al. (1988) measured excursions of wall shear stress reaching up to $\tau_{w,rms} = 0.4\overline{\tau_w}$ in wall-bounded flows and Schlatter and Örlü (2010) proposed a variation with Reynolds number according to: $\tau_{w,rms}/\overline{\tau_w} = 0.298 + 0.018\ln(Re_\tau)$. Using the latter, converted to excursions of friction velocity ($U_\tau = \sqrt{\tau_w/\rho}$), for simplicity assumed linear, corresponding to a linear increase in U_f, one can get a rough estimate of the expected d_b variation with U_f based on the adapted KH theory. The result agrees well with the variation of the measured mean (red solid and black dashed line respectively, in Fig. 6, middle panel). While the simple relationship above is unlikely to accurately estimate U_τ due to the inherent complexity of such flows, the overall trends are representative. Thus, they allow us to connect the size of bubbles with the local wall-shear just upstream of where they are formed: an increase of the latter within established limits for wall-turbulence, is sufficient to explain the measured decrease in the corresponding average bubble size.

The spatial correlations discussed in the previous paragraphs did not make use of the datasets' temporal resolution, and thus do not necessarily guarantee a correlation between the incoming flow time evolution and that of the air coverage downstream. For this reason, we also assess the correlation between the temporal evolution of the liquid velocity profile closest to the injector $U_f(x_i, z)$ ($x_i = -0.6\delta$) and that of the wall-projected air coverage immediately downstream of the injector, $\langle A_w \rangle_{l_x}$ (see Fig. 7(b) for an example of their respective spanwise profiles). The air coverage, due to its binary nature and topology is averaged over a certain streamwise distance (red shaded area, Fig. 7(a), right), so that it incorporates the larger air pockets closest to the injector ($\overline{A_w}$, Fig. 5(b)). It is expected that the optimal

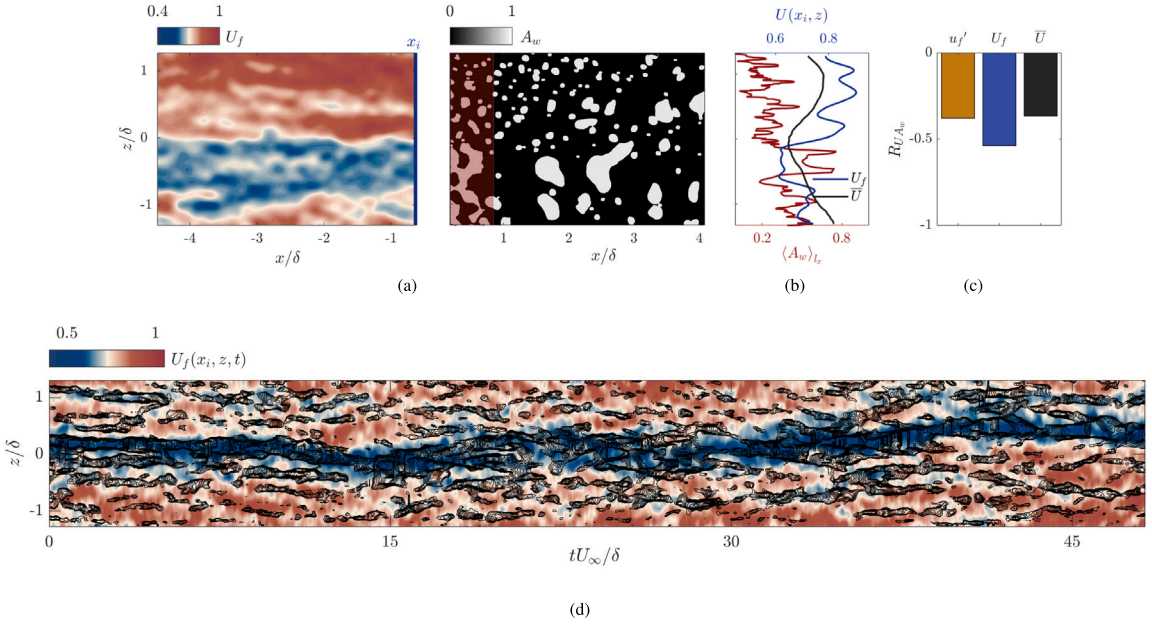

Fig. 7. Liquid TBL and bubbly regime (Case B1) - (a) Time evolution of $U_f(x_i, z)$ (left, blue solid line), is correlated with that of the wall-projected air coverage A_w, averaged over l_x (right, shaded in red). (b) Instantaneous profiles of $U(x_i, z)$, $\overline{U}(x_i, z)$, and $\langle A_w \rangle_{l_x}$ corresponding to (a). (c) Resulting correlation values averaged over all time-resolved sets. (d) $U(x_i, z, t)$ contours for a single set, $\langle A_w \rangle_{l_x}$ overlaid in black, for values ranging from 0.4 to 1.0, at steps of 0.05. All velocities are outer-normalised. (For interpretation of the references to colour in this figure legend, the reader is referred to the web version of this article.)

l_x for the temporal correlation of the two phases is dependent on the air bubble/pocket size, an observation we will return to in the analysis of the transitional regime (Case B2), where larger pockets of air are present. For the bubbly regime, we find that the anti-correlation $-R_{U_f \langle A_w \rangle_{l_x}}$ is maximised for $l_{x,B1} = 0.67\delta$ (see Fig. A.12 and discussion in Appendix A), a length comparable to the average extent of the air pocket almost always attached to the injector (as seen in the contours of $\overline{A_w} > 0.6$ in Fig. 5(b)), and it is used in the results presented here. Regardless of that choice however, $R_{U_f \langle A_w \rangle_{l_x}}$ values are statistically significant for almost all l_x tested ($R_{U_f \langle A_w \rangle_{l_x}} < -0.2$), underlining the distinct effect of the incoming flow velocity on the air coverage downstream. Examining the correlation coefficients averaged over all time-resolved sets, it is again clear that U_f, incorporating the spanwise inhomogeneity of both $\overline{U}$ and u', is the most accurate predictor of the three for the air coverage downstream, with $R_{U_f \langle A_w \rangle_{l_x}} = -0.5$ (Fig. 7(c)). A visual representation of this temporal correlation between liquid and gas can be seen for one time-resolved dataset in Fig. 7(d).

3.2.2. *Transitional regime — case B2*

When the air flow rate Q_{air} is increased, air bubbles start to coalesce faster and larger pockets start to form (see Fig. 8(a)). Air pockets attached at the injector cover a significantly larger area, are elongated in x and indicate a shedding behaviour over time rather than being convected downstream (see supplementary video S2); however, there is still no spanwise constant air layer formed, so this regime is often termed *transitional* (transition towards an air layer). With respect to the liquid-gas interactions which we are interested in, the focus here will be on the level of influence of the upstream TBL organisation on the area coverage achieved by the air phase; TBL structures that are positively correlated with air coverage would promote transition to an air layer, while those negatively correlated would be inhibitors. This is a regime for which the resulting drag reduction is seen to increase linearly with Q_{air} (Elbing et al., 2008) and given the well-established difficulties in maintaining an intact air layer during intense ship motions, it is likely also the most frequent regime throughout a vessel's journey; as such it is also crucial from an application perspective, despite being less investigated overall.

The analysis in this regime is similar to what was described in the previous section for Case B1, with the main difference being that here we focus solely on the wall-projected air coverage A_w. Independently tracking the larger pockets of air convected downstream is out of scope of the present study: they represent a small percentage of the total air coverage and due to their large deformability, tracking their centre to estimate their convection velocity would no longer be representative. The total air coverage, A_w, is estimated by an image processing algorithm, identifying the air phase edges from the raw shadowgraphy images based on intensity differences and then, after a series of dilation, erosion, and filling operations, resulting in a binary separation of the air ($A_w = 1$) and liquid phases ($A_w = 0$); an instantaneous example can be seen in Fig. 8(a). Internal (liquid filled) gaps of the larger air pockets are separately identified and excluded, and while there are still some artefacts remaining due to the inherent difficulty in their detection, especially close to the injector, these do not meaningfully affect any of the conclusions drawn here.

We first examine the average incoming velocity field, $\overline{U}(x, z)$ and the corresponding average downstream air coverage, $\overline{A_w}$ (Fig. 8(b)). Similar to Case B1, the spanwise variation of the former affects significantly the topology of the latter, with air pockets almost always formed ($\overline{A_w} > 0.8$) downstream of regions of low $\overline{U}$ ($z = 0$), albeit here, their streamwise extent ($\approx 1.5\delta$) is almost double the one in case B1, owing to the higher Q_{air} injected and the larger pockets formed overall. The shape of the $\overline{A_w}$ contours also exhibits a monotonic decrease in coverage for locations away from the mid-span, indicating that smaller air pockets that have pinched off and convect downstream are more frequent or that the air pocket still attached to the injector has a much shorter streamwise extent in those regions, or both (also visually observed in the supplementary video S2). Finally, the mean liquid flow exhibits again a deceleration closer to the injector, due to the adverse pressure gradient effect of the air-induced blockage (which is higher than in case B1, as expected due to the larger amount of air injected).

Subsequently, we investigate the correlation between the instantaneous incoming flow and the air coverage, over time. The streamwise liquid velocity is filtered (U_f, see Fig. 9(a), left) as described in Case B1 (2D Gaussian, with $\sigma = 2$ and a kernel size equal to the extents of $R_{u'u'} = 0.25$), in order to isolate the large-scale liquid velocity effects on

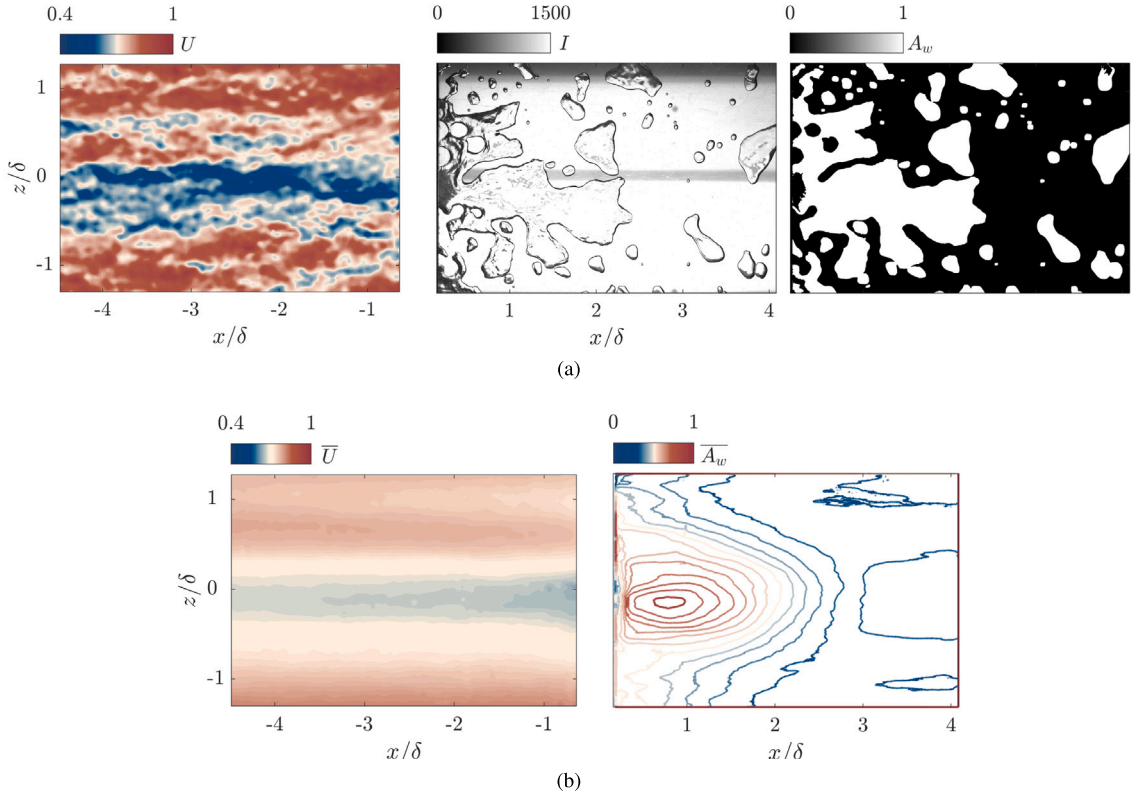

Fig. 8. Liquid TBL and transitional regime (Case B2) (a) Instantaneous liquid velocity (left), air phase (middle), and corresponding wall-projected area A_w (right). (b) Mean liquid velocity (left), and $\overline{A_w}$ for all datasets (right).

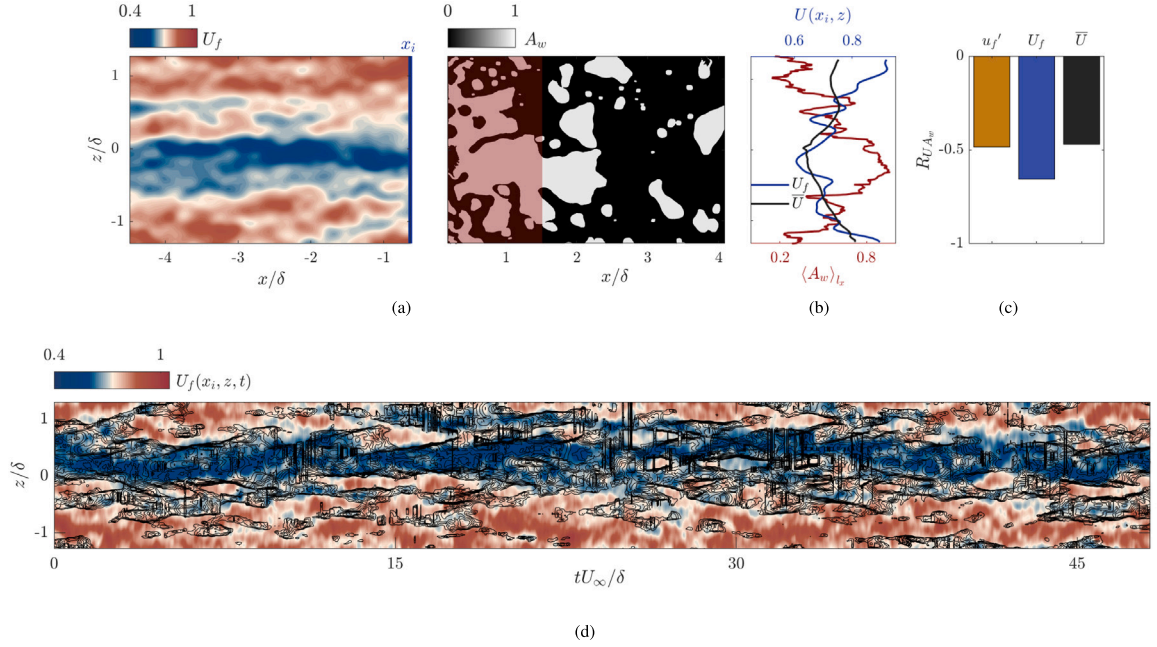

Fig. 9. Liquid TBL and transitional regime (Case B2) (a) Time evolution of $U_f(x_i, z)$ (left, blue solid line), is correlated with that of the wall-projected air coverage A_w, averaged over l_x (right, shaded in red). (b) Instantaneous profiles of $U_f(x_i, z)$, $\overline{U}(x_i, z)$, and $\langle A_w \rangle_{l_x}$ corresponding to (a). (c) Resulting correlation values averaged over all time-resolved sets. (d) $U(x_i, z, t)$ contours for a single set, $\langle A_w \rangle_{l_x}$ overlaid in black, for values ranging from 0.5 to 1.0, at steps of 0.05. All velocities are outer-normalised. (For interpretation of the references to colour in this figure legend, the reader is referred to the web version of this article.)

the gas topology. The time evolution of the spanwise profile of the latter closest to the injector, $U_f(x_i, z)$ ($x_i = -0.6\delta$) is correlated to that of the wall-projected air coverage immediately downstream of the injector, $\langle A_w \rangle_{l_x}$ (see Fig. 9(b) for an example). As mentioned in the previous section, the air coverage profile, due to its binary nature and topology, is averaged over $l_{x,B2} = 1.5\delta$ (shaded red region in Fig. 9(a), right) in order to properly incorporate its streamwise length scale. This distance, found to maximise the (anti-) correlation between air coverage and

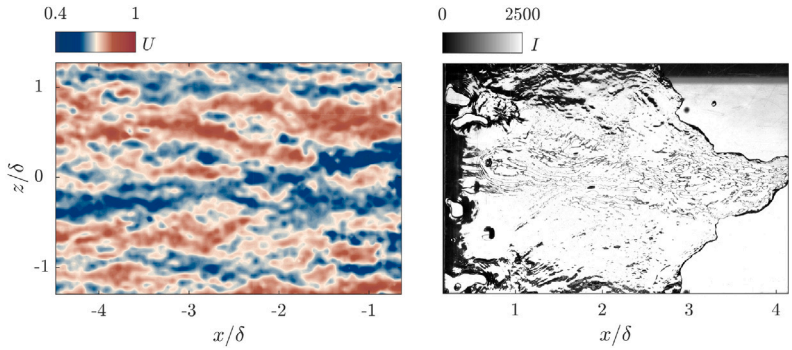

Fig. 10. Liquid TBL and air layer regime (Case B3) Instantaneous liquid velocity (left) with the corresponding air layer topography downstream of the injector (right). There is indication of shedding in the mid-span of the domain and of liquid pockets 'breaking up' the air continuity close to the injector (see also supplementary video S3).

upstream liquid velocity, is approximately twice the one found for the bubbly regime (see also Fig. A.12 in Appendix A), and agrees well with the average extent of the air pocket almost always present close to the injector ($\overline{A_w} > 0.7$ in Fig. 8(b)). This result highlights the dependence of l_x on the spatial scale of the air phase ($l_{x,B2} > l_{x,B1}$) and represents the streamwise distance along which the air phase is the most sensitive on the upstream TBL. Regardless, for all l_x tested, U_f and $\langle A_w \rangle_{l_x}$ were found to be significantly anti-correlated in time, emphasising the importance of the instantaneous upstream flow conditions. When averaged over all time-resolved datasets, the (filtered) instantaneous velocity, U_f was again found to be the one most negatively correlated with the downstream air coverage ($R_{U_f \langle A_w \rangle_{l_x}} = -0.65$), when compared to the correlations using the spanwise profiles of either the turbulent fluctuations or the mean velocity alone ($R_{u' \langle A_w \rangle_{l_x}} = R_{\overline{U} \langle A_w \rangle_{l_x}} = -0.48$, see Fig. 9(c)).

These results illustrate that the large-scale instantaneous organisation of the incoming TBL streamwise velocity affects the downstream air coverage substantially (see Fig. 9(d) for their correlation in a single time-resolved dataset), incorporating the significant (but lower) contributions of the spanwise inhomogeneity of both the turbulent fluctuations as well as the mean velocity in that plane. As mentioned previously, in canonical conditions, where the mean velocity is homogeneous in z, it would solely be the large-scale organisation of u' which would be able to affect the air downstream, and, given its already significant contribution in our case, where the mean also plays a role, it is safe to assume that the effect would also be substantial. Aside from these distinctions, another important conclusion here is that of the log-region residing coherent structures, high-speed streaks in the upstream TBL are inhibitors of air coalescence, and thus of the transition to an air layer regime, while low-speed ones locally facilitate it.

3.2.3. *Air layer regime — case B3*

Finally, we turn our attention to the last air phase regime examined here, the air layer regime, achieved for the highest employed Q_{air} (see also Table 1). It should be noted here that, the term *air layer* for these flow conditions might be arguable, given the limited streamwise extent of the formed cavity. In similar studies, sometimes the term *air cavity* is alternatively used (see Nikolaidou et al., 2024; Anand et al., 2025, for example); we chose the former for emphasis on the spanwise continuity of the regime and not to imply an air layer covering the full plate in length. Besides, we do consider the liquid-gas interactions described here robust enough to also apply to the formation of longer air layers in higher freestream velocities.

In this regime, the injected air forms a spanwise-stable layer on the plate (see Figs. 2 and 10, right), which, despite dynamic shedding in the mid-span (and on the sides, not seen here due to the limited FOV), retains an almost constant (minimum) streamwise extent (see also supplementary video S3 and discussion in Nikolaidou et al., 2024). Thus in these conditions, the air phase, due to the high air flow rate imposed, has overcome any inhomogeneity in the incoming TBL to form an air layer. The incoming flow however, might still influence the topology of the air phase, for example in the form of liquid pockets, which are locally 'breaking' the continuity of the air layer at seemingly random spanwise locations (see the region close to the injector in Fig. 10, right). Such liquid pockets have been observed in the other regimes as well, but since no air layer was formed there, they were not marked as breakup events. Given the up-till-now established negative correlation of air coverage with the upstream velocity magnitude, these liquid pockets are then expected to be positively correlated with high-speed streaks in the liquid TBL; our focus in this section is to establish, and quantify where possible, this correlation. Aside from the fundamental implications of such analysis, these air layer gaps are also crucial from an application standpoint: they are responsible for local breakups of the drag reducing air-layer, potentially impacting its performance and also establishing 'hot-spots' for further/more severe breakups in more adverse sea conditions.

The SDG snapshots of the air layer regime were thus processed in order to identify these liquid pockets, most often found close to the injector: the outside envelope of the air layer edge was identified first, including any internal, fully connected regions. The latter include intensity variations due to the free-surface deformations of the air layer as well as the sought-after liquid pockets. These were distinguished based on their streamwise location (originating at the first half of the FOV in x), the smoothness of their edges (employing curvature values), their high intensity background (liquid filled), and their time continuity. An instantaneous example can be seen in Fig. 11(a), middle, with the identified liquid pockets shaded in cyan. Due to unfavourable illumination conditions, especially at the edges of the FOV and around the injector, not all pockets could be detected, however the algorithm achieved a very low percentage of false positives (< 1%), allowing us to draw accurate conclusions about their characteristics and dependence on the upstream TBL. Specifically, we registered the location of their centre in x (x_g) and z (z_g, to allow correlations with the upstream flow), and their streamwise and spanwise extents, $l_{g,x}$ and $l_{g,z}$, respectively (see also Fig. 11(a), middle). The liquid TBL velocity on the other hand was spatially filtered with a 2D Gaussian to remove small-scale variations (same as in cases B1 and B2 above, see U_f in Fig. 11(a), left).

Results indicate that the streamwise and spanwise extents of the liquid pockets are very similar, with $\overline{l_{g,x}} = \overline{l_{g,z}} = 0.2\delta$, thus generally exhibiting circular shapes (Fig. 11(a), right). Instantaneously, the pockets can get much longer ($> 0.6\delta$), while their spanwise extent has a more limited range ($0.1\delta < l_{g,z} < 0.4\delta$) with the most frequent value being equal to the mean; the latter is also comparable to the average spanwise extent of the velocity streaks upstream (equal to 0.22δ for $R_{u'u'} = 0.25$, Fig. 3(c)), a fact supportive of the notion that the two might be correlated. In terms of their streamwise location, these breakup events are on average centred close to the injector ($\overline{x_g} < 0.1\delta$, Fig. 11(b)), and none of them at distances $x_g > 0.2\delta$. It should be noted that, once they form, the pockets can grow in size while still being

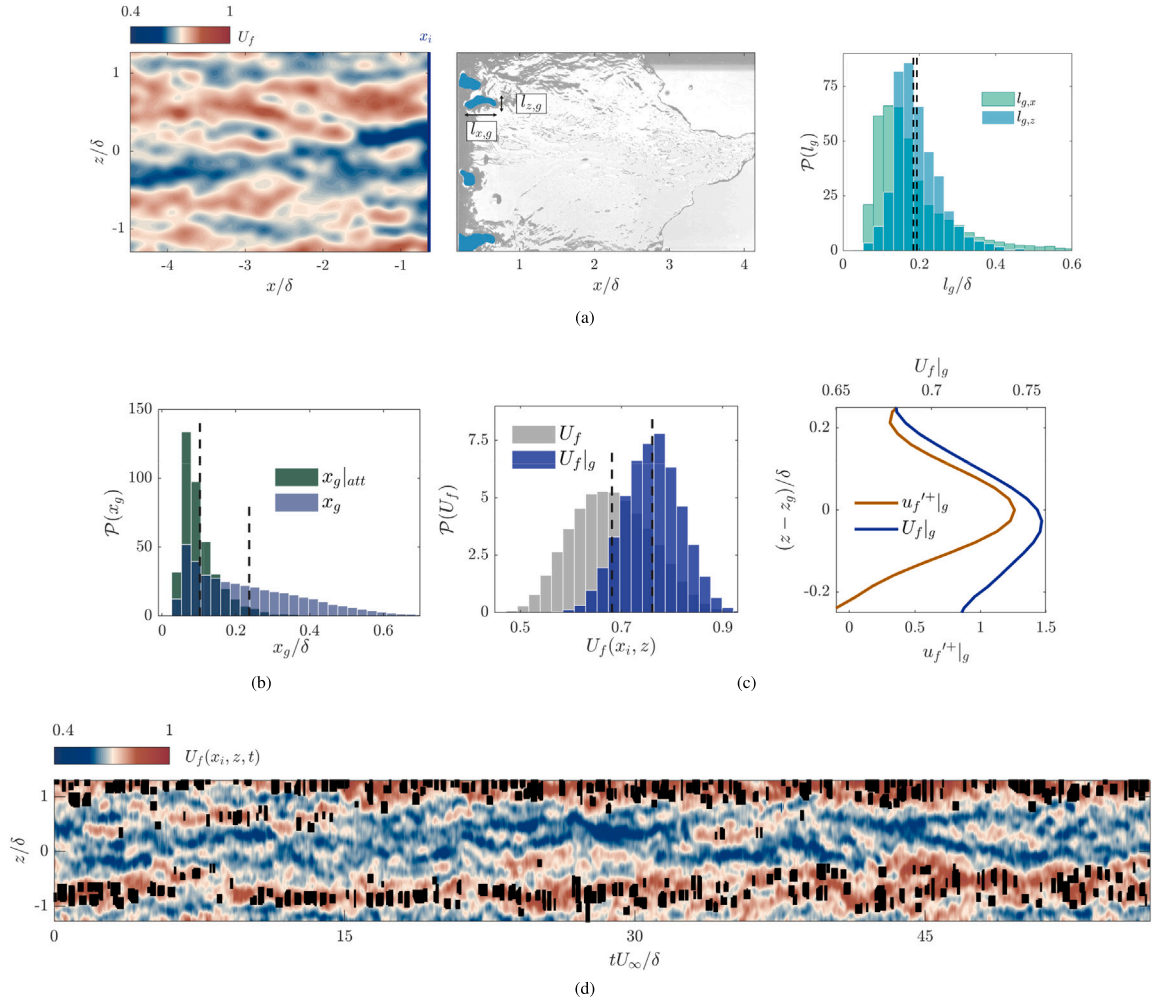

Fig. 11. Liquid TBL and air layer regime (Case B3) (a) Filtered liquid streamwise velocity U_f (left panel) with corresponding liquid pockets in the air layer (middle panel, shaded in cyan), and the p.d.f. of their spatial extents (right panel). (b) P.d.f. of the streamwise location of the centres of all detected liquid pockets, x_g, and of its subset, $x_g|_{att}$ (liquid pockets still attached to the injector). (c) P.d.f. (left panel) of $U_f(x_i, z)$ and of its subset $U_f(x_i, z)|_g$ (conditioned on the presence of a liquid gap downstream), and the conditionally averaged profile of the later, together with $u_f{}'(x_i, z)|_g$, for all snapshots (right panel). (d) $U_f(x_i, z, t)$ contours for a single time-resolved set, with the detected liquid pockets overlaid in black. All velocities are outer-normalised, except for u', which is normalised using U_τ. Mean values of p.d.f distributions indicated with dashed vertical lines.

attached to the injector, or pinch-off and convect downstream before being ingested in the air layer (see also supplementary video S3). In what follows, we only focus on whether a liquid pocket can develop (or continue to grow) while still attached to the injector, because we deem this directly associable with the upstream conditions. Thus, we only consider those pockets still attached to the injector (see $\mathcal{P}(x_g|_{att})$ in Fig. 11(b)).

In order to probe this correlation statistically, we first examine the spanwise profile of the liquid velocity closest to the injector, $U_f(x_i, z)$ ($x_i = -0.6\delta$, see blue solid line in Fig. 11(a), left). When comparing all possible velocity values at this streamwise location (with an average of $0.68U_\infty$), with those only at spanwise locations where a liquid pocket exists downstream ($U_f|_g$), it is clear that the range of the latter is distinctly shifted to much higher values (see p.d.f. in Fig. 11(c), left) and its average is also significantly higher ($0.76U_\infty$). Although a clear overlap does exist between the two velocity distributions, such that a specific upstream velocity cannot exclude nor guarantee the presence of a breakup, there have been no identified air layer breakups downstream of points where $U_f < 0.6U_\infty$. While the above support a positive correlation between high-speed liquid flow and air layer gaps, they do not provide information on whether the former is actually spatially coherent (i.e. part of a high-speed streak). Thus, we also look at the conditional (spanwise) profile of $U_f|_g$ around these liquid pockets. For each detected pocket, the corresponding upstream velocity at distances $z = z_g \pm 0.2\delta$ is averaged, leading to a conditional profile centred at $z = z_g$ (see Fig. 11(c), right). This profile indicates a clear global maximum at $z = z_g$, highlighting the spanwise coherence of the liquid TBL upstream of these air layer breakups, as well as its spanwise alignment with them. The same behaviour is also observed for the conditionally averaged turbulent fluctuation profile ($u_f{}'(x_i, z)|_g > 0$); the underlying spatially varying mean notwithstanding, such observations reinforce the notion that these breakup events are not (solely) due to a mean velocity variation, but are manifestations of intense high-speed fluctuations whose spatial coherence and amplitude are sufficient to locally affect the air phase topology. Finally, when examining the time evolution of $U_f(x_i, z)$ and the location of detected air layer breakups (denoted in black in Fig. 11(d), for a single time-resolved dataset), it becomes evident that the spatial alignment of the two in z is also coherent over time, with the appearance of the latter following the meandering behaviour of high-speed streaks of the TBL. It should be noted here that $U_f(x_i, z, t)$ exhibits slightly lower values compared to Cases B1 and B2, due to an increase in air blockage, manifesting as a local deceleration, affecting the most downstream PIV locations, and thus x_i in particular (see Fig. 3(a) and also the relevant discussion in Nikolaidou et al. (2024)). Regardless, there are only marginal differences in both the underlying turbulence statistics (dashed lines in Figs. 3(a) and 3(b) and Figs. 3(c) and 3(d)) as

well as the mean spanwise variation (solid lines in Figs. 3(a) and 3(b)) in all cases, indicating that the turbulent flow organisation upstream of the air injection remains mostly unaltered when air is injected. For completeness, the corresponding $u_f(x_i, z, t)$ fields from Figs. 7(d), 9(d), and 11(d), are also presented in Appendix B (Fig. B.13), further supporting that notion from an instantaneous perspective.

4. Discussion

In the previous sections we examined the correlation between the liquid flow upstream of the air injection and the downstream air phase topology, in the three different regimes typically defined in air lubrication studies. Such an analysis of the air phase, as it transitions from a bubbly regime to an air layer, as well as the time resolution available for both phases, allow us to propose a global picture of the causal relationship between the two. However, before elaborating on this aspect, it is important to first point out some inherent limitations of our study.

First, our analysis has been limited to planar imaging. With respect to the air phase, the implications are somewhat limited. Using planar imaging and ensuring sufficient focus, needed for image segmentation, the lack of 3D information is mainly reflected in the following choices: using the equivalent bubble diameter d_b to represent the overall bubble size, and the centre of the bubble's wall-projected area as the overall centre of mass for velocity estimates, neglecting any possible height variations. Given the liquid shear dominance on the bubble shape and the type of analysis presented here (focused on correlations between phases and not on absolute air phase characteristics), we do not consider this a limiting factor for the conclusions herein. For the liquid phase, given the wall-normal inhomogeneity of TBL, a further comment is warranted. As mentioned in Section 2, we selected the PIV wall-parallel plane ($y = 0.1\delta$) such that it coincides with the maximum expected height of the air layer, and we specifically chose the scale ratio to be such that the air phase would be entirely within the logarithmic region of the TBL; large-scale coherent structures residing there are known to span the majority of the TBL thickness (see Hutchins and Marusic, 2007b, among others). Thus, we consider the spanwise variation of U at a wall-parallel slice within the log region to be representative of the inhomogeneity that the air phase will experience throughout y, the mean shear notwithstanding. The strong correlations reported here reinforce that notion, although the imprint of the mean shear on the air phase, especially for a variety of scale ratios, is a topic deserving further attention in future studies. 3D data of the liquid flow would also provide information on the wall-normal component of velocity, which is expected to be important on the air phase dynamics as well (Anand et al., 2025).

Second, as mentioned in various points throughout the results section, our departure from canonicality due to the presence of a spatially varying mean, although not itself limiting, does affect the observed phenomena. An effort was made to separate the effects of the mean and instantaneous spanwise variation, and results indicate that although the former has an influence on the air phase characteristics, the instantaneous velocity, which includes turbulent fluctuations, provides consistently enhanced correlations, especially with respect to temporal evolution. Further, even using the fluctuating fields themselves still leads to statistically significant correlations with the air phase topology, suggesting that their magnitude and spatial coherence are sufficient to locally affect the air phase, even in canonical conditions, i.e. where they are the sole source of the flow's spanwise inhomogeneity. Thus, we consider all conclusions made here regarding the spanwise variation of instantaneous velocity directly applicable to the spanwise organisation of velocity fluctuations in canonical cases.

Lastly, we need to reiterate that our focus is on the effects of the upstream flow alone; causal relationships with the air phase are inferred solely within this context. Effects of surface tension, presence of contaminants, and bubble-bubble interactions are thus not considered. To a certain extent we assume their importance in the dynamics discussed to be limited compared to upstream flow organisation, however this is not (directly or indirectly) assessed and is another topic warranting further exploration in future studies.

With these limitations in mind, here we propose a unified description of the interaction between the liquid TBL upstream of the injector and the air phase downstream, as the air flow rate increases and the air transitions from individual bubbles to larger pockets and finally an air layer. For a low Q_{air} and a slot-type injector without any porous material included or cavitator present, individual bubbles are formed, with an average diameter $\overline{d_b}$ overlapping with the maximum stable size predicted by the Kolmogorov-Hinze (KH) theory, as adapted for a wall-bounded flow (Sanders et al., 2006). The distribution around $\overline{d_b}$ is imposed to a substantial extent by the instantaneous spanwise organisation of the incoming TBL: larger, slow moving bubbles can only be formed downstream of low-speed streaks while bubbles formed downstream of high-speed ones are always smaller and correspondingly faster. We suggest that the variation in bubble size is due to the instantaneous variation in U_τ, which is known to follow that of U (Hutchins et al., 2011; Gomit et al., 2020; Guerrero et al., 2020, among others) and can reach up to $\pm 0.4\overline{U_\tau}$. This is sufficient for a d_b variation with U, as predicted by the TBL-adapted KH theory, which agrees with the experimentally measured one. The above effects become less pronounced at large downstream distances from the injector ($x > 4\delta$) although due to the long streamwise coherence, a significant influence of the upstream flow remains, especially for U_b. The total air coverage of the plate follows the meandering behaviour of the low-speed streaks over time, for distances at least up to 1δ downstream of the injector, highlighting that there is also a temporal correlation between bubble size and U. Despite a similar deterioration of this effect away from the injector, its importance is crucial: this is the area where coalescence starts to prevail at higher air flow rates and the spanwise continuity of the air layer starts developing. Larger air pockets are then formed, several of which still pinching off from the injector and convecting downstream; the largest pocket typically remains attached to the injector however, exhibiting some semi-periodic shedding around $x = 2\delta$. We stipulate that as air flow rate increases, larger air pockets are affected by the local variation in U – and thus wall-shear – in a similar way as bubbles, albeit with a much higher chance of remaining attached to the injector. That is indeed reflected in the topology of the air coverage in this regime, which follows even more distinctly the low-speed streak meandering (higher correlation) and for larger distances (up to 2–3δ downstream of the injector) compared to the bubbly one. This has two main implications: first, that the streamwise distance over which the incoming flow dictates the air coverage topology increases with Q_{air} as we move from the bubbly to the transitional regime, and second, that upstream low-speed streaks are indeed local facilitators of air coalescence and spatial continuity, while high-speed ones are inhibitors. This causal relationship continues even when Q_{air} is increased to the point that a spanwise continuous layer has formed. It manifests itself in local breakups of the air layer, starting at the injector and propagating downstream; these are a direct consequence of spanwise aligned high-speed streaks upstream of the injector and could lead to a complete breakdown of the air layer continuity at more adverse conditions. However, in contrast to the transitional regime, an increase in Q_{air} is expected to curtail this TBL influence, with the wetted pockets becoming smaller and remaining closer to the injector (see also Nikolaidou et al., 2024). It should also be noted here that, due to the meandering behaviour of log-region streaks, the spanwise location of these pockets varies in time, while breakup events always forming at the same spanwise location would be an indication of a fixed upstream disturbance instead, such as roughness.

5. Conclusions

In this work, we experimentally assessed the effect of spanwise inhomogeneity of the streamwise velocity in turbulent boundary layers (TBLs) on air lubrication, by simultaneously measuring both liquid and gas phases using high-speed PIV and shadowgraphy, respectively. While keeping a constant U_∞, the spatial extent and dynamics of air pockets deeply embedded within the TBL are significantly impacted by its instantaneous organisation for all regimes examined (bubbly, transitional, air layer). Specifically, low-speed streaks known to populate the logarithmic region are shown to be facilitators of larger bubble formation and their meandering in time is a good predictor of air coverage for the bubbly and transitional regimes. High-speed streaks on the other hand, locally inhibit the formation of larger air pockets and thus of a spanwise continuous air layer, and even when one is formed, they are largely responsible for local breakup events. The above effects were shown to be relevant for large streamwise distances downstream of the injector (ranging from 1δ to 4δ) and while a systematic scaling analysis of this zone of influence was out of scope of this work, it is evident that TBL length scales and Q_{air} are relevant parameters.

Given the vast knowledge accumulated over the years on scaling of turbulent coherent structures, these insights on the sensitivity of the air phase on the incoming flow are of significant value for our understanding of air lubrication in full-scale, realistic conditions, where instantaneous flow inhomogeneity is expected due to both turbulence and surface roughness, and air layer coverage and stability are critical from an application perspective.

Declaration of competing interest

The authors declare that they have no known competing financial interests or personal relationships that could have appeared to influence the work reported in this paper.

Acknowledgements

The author gratefully acknowledges Edwin Overmars and Jasper Ruijgrok for assistance in setting up the experiments and Christian Poelma and Lina Nikolaidou for the insightful discussions.

Appendix A. Streamwise averaging of air coverage, $\langle A_w \rangle_{l_x}$

For the correlation between the time evolution of the incoming liquid flow profile ($U_f(x_i, z, t)$ with $x_i = -0.6\delta$), and the downstream air coverage (A_w), the spanwise profile of the latter is averaged over a streamwise distance l_x downstream of the injector, in order for its spatial topology to be properly incorporated.

For both the bubbly (Case B1) and the transitional regime (Case B2), a range of streamwise distances is examined ($0 \leq l_x \leq 4\delta$), and the resulting correlation coefficient $R_{U_f\langle A_w\rangle_{l_x}}$ is assessed (Fig. A.12). It is evident that, regardless of regime, U_f and $\langle A_w \rangle_{l_x}$ are negatively correlated for all l_x tested, highlighting the alignment of air coverage with low-speed velocity streaks. The two cases also exhibit a similar trend of an initial decrease towards a (wide) global minimum, before increasing again as averaging effects weaken the correlation. The optimal l_x at which $R_{U_f\langle A_w\rangle_{l_x}}$ is minimised, increases twofold from the bubbly ($l_{x,B1} = 0.7\delta$) to the transitional regime ($l_{x,B2} = 1.5\delta$), underlining the effect of the air pocket size on the extent of the TBL influence. For all l_x values larger than the optimal, this negative correlation is consistently stronger in the transitional regime, and remains significant even when A_w is averaged throughout the FOV ($R_{U_f\langle A_w\rangle_{l_x}} = -0.44$). On the other hand, when A_w is averaged over short distances ($l_x < 0.5\delta$), the resulting correlation with U_f is stronger in the bubbly regime, likely owing to the more limited streamwise coherence of A_w in that case.

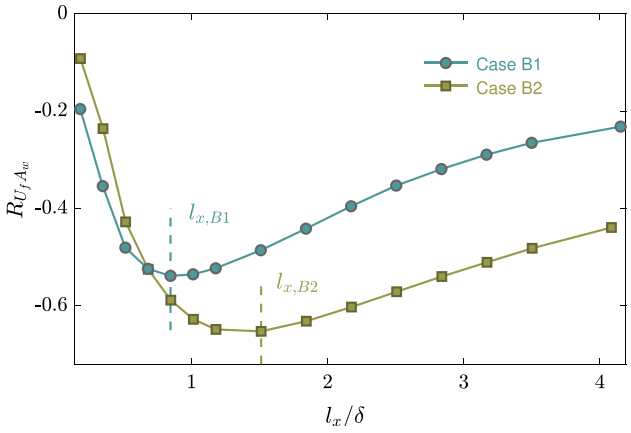

Fig. A.12. Cases B1 and B2.

Appendix B. Time evolution of turbulent fluctuations, $u_f(x_i, z, t)$

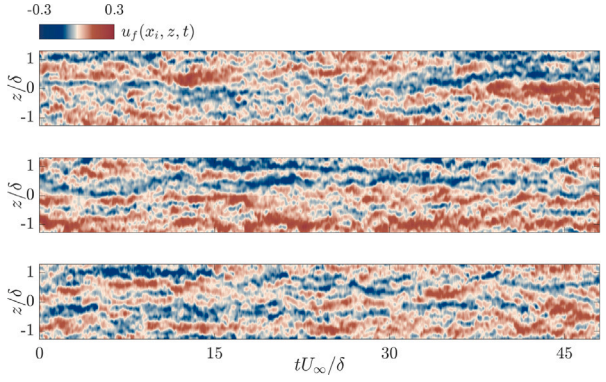

Fig. B.13. $u_f(x_i, z, t)$ contours (outer normalised) for the time-resolved sets in Figs. 7(d) (Case B1 — top), 9(d) (Case B2 — middle), and 11(d) (Case B3 — bottom).

The time evolution of the turbulent fluctuations at the most downstream location, x_i of the PIV FOV, $u_f(x_i, z, t)$, corresponding to the full velocity fields $U_f(x_i, z, t)$ from Figs. 7(d), 9(d), and 11(d), is presented here for completeness, to further highlight the similarity of the resulting flow fields upstream of the injection, regardless of air injection rate (see Fig. B.13).

Appendix C. Supplementary data

Supplementary material related to this article can be found online at https://doi.org/10.1016/j.ijmultiphaseflow.2025.105383.

Data availability

Data will be made available on request.

References

Alfredsson, P.H., Johansson, A.V., Haritonidis, J.H., Eckelmann, H., 1988. The fluctuating wall-shear stress and the velocity field in the viscous sublayer. Phys. Fluids 31, 1026–1033.

Anand, A., Nikolaidou, L., Laskari, A., Poelma, C., 2025. Turbulent boundary development over an air cavity. Flow 5, E2.

Ceccio, S.L., 2010. Friction drag reduction of external flows with bubble and gas injection. Annu. Rev. Fluid Mech. 42, 183–203.
De Silva, C.M., Kevin, K., Baidya, R., Hutchins, N., Marusic, I., 2018. Large coherence of spanwise velocity in turbulent boundary layers. J. Fluid Mech. 847, 161–185.
Deike, L., 2022. Mass transfer at the ocean–atmosphere interface: The role of wave breaking, droplets, and bubbles. Annu. Rev. Fluid Mech. 54, 191–224.
Dennis, D.J.C., Nickels, T.B., 2008. On the limitations of taylor's hypothesis in constructing long structures in a turbulent boundary layer. J. Fluid Mech. 614, 197–206.
Dennis, D.J.C., Nickels, T.B., 2011. Experimental measurement of large-scale three-dimensional structures in a turbulent boundary layer. Part 2. Long structures. J. Fluid Mech. 673, 218–244.
Deutsch, S., Castano, J., 1986. Microbubble skin friction reduction on an axisymmetric body. Phys. Fluids 29, 3590–3597.
Elbing, B.R., Winkel, E.S., Lay, K.A., Ceccio, S.L., Dowling, D.R., Perlin, M., 2008. Bubble-induced skin-friction drag reduction and the abrupt transition to air-layer drag reduction. J. Fluid Mech. 612, 201–236.
Ferrante, A., Elghobashi, S., 2004. On the physical mechanisms of drag reduction in a spatially developing turbulent boundary layer laden with microbubbles. J. Fluid Mech. 345–355.
Gabillet, C., Colin, C., Fabre, J., 2002. Experimental study of bubble injection in a turbulent boundary layer. Int. J. Multiph. Flow 553–578.
Gomit, G., de Kat, R., Ganapathisubramani, B., 2020. Structure of high and low shear-stress events in a turbulent boundary layer. Phys. Rev. Fluids 3, 014609.
Guerrero, B., Lambert, M.F., Chin, R.C., 2020. Extreme wall shear stress events in turbulent pipe flows: spatial characteristics of coherent motions. J. Fluid Mech. 904, A18.
Harleman, M.J.W., Delfos, R., van Terwisga, T.J., Westerweel, J., 2011. Dispersion of bubbles in fully developed channel flow. J. Phys. Conf. Ser. 052007.
Hinze, J.O., 1955. Fundamentals of the hydrodynamic mechanism of splitting in dispersion processes. AIChE J. 1, 289–295.
Hutchins, N., Marusic, I., 2007a. Evidence of very long meandering features in the logarithmic region of turbulent boundary layers. J. Fluid Mech. 579, 1–28.
Hutchins, N., Marusic, I., 2007b. Large-scale influences in near-wall turbulence. Phil. Trans. R. Soc. A 365, 647–664.
Hutchins, N., Monty, J.P., Ganapathisubramani, B., Ng, H., Marusic, I., 2011. Three-dimensional conditional structure of a high-Reynolds-number turbulent boundary layer. J. Fluid Mech. 673, 255–285.
Kevin, K., Monty, J., Hutchins, N., 2019. The meandering behaviour of large-scale structures in turbulent boundary layers. J. Fluid Mech. 865, R1.
Kim, S., Oshima, N., Park, H.J., Murai, Y., 2021. Direct numerical simulation of frictional drag modulation in horizontal channel flow subjected to single large-sized bubble injection. Int. J. Multiph. Flow 145, 103838.
Kim, Y.R., Steen, S., 2023. Potential energy savings of air lubrication technology on merchant ships. Int. J. Nav. Arch. 15, 100530.
Kolmogorov, A., 1949. On the breakage of drops in a turbulent flow. Dokl. Akad. Navk. SSSR 66, 825–828.
Latorre, R., Miller, A., Philips, R., 2009. Micro-bubble resistance reduction on a model SES catamaran. Ocean Eng. 2297–2309.
Lo, T., L'vov, V.S., Procaccia, I., 2006. Drag reduction by compressible bubbles. Phys. Rev. E 73, 036308.
Lu, J., Fernández, A., Tryggvason, G., 2005. The effect of bubbles on the wall drag in a turbulent channel flow. Phys. Fluids 17 (9), 095102.
Madavan, N., Deutsch, S., Merkle, C.L., 1985. Measurements of local skin friction in a microbubble-modified turbulent boundary layer. J. Fluid Mech. 156, 237–256.
Magnaudet, J., Eames, I., 2000. The motion of high-Reynolds-number bubbles in inhomogeneous flows. Annu. Rev. Fluid Mech. 32, 659–708.
Masuk, A.U.M., Ashwanth, K.R., Ni, R., 2021. Simultaneous measurements of deforming Hinze-scale bubbles with surrounding turbulence. J. Fluid Mech. 910, A21.
McCormick, V., Bhattacharyya, R., 1973. Drag reduction of a submersible hull by electrolysis. Nav. Eng. J. 85, 11–16.
Murai, Y., 2014. Frictional drag reduction by bubble injection. Exp. Fluids 55, 1173.
Nikolaidou, L., Laskari, A., van Terwisga, T., Poelma, C., 2024. Effect of incoming flow conditions on air lubrication regimes. Int. J. Multiph. Flow 180, 104948.
Oishi, Y., Murai, Y., 2014. Horizontal turbulent channel flow interacted by a single large bubble. Exp. Therm. Fluid Sci. 55, 128–139.
Park, H.J., Tasaka, Y., Murai, Y., 2019. Bubbly drag reduction investigated by time-resolved ultrasonic pulse echography for liquid films creeping inside a turbulent boundary layer. Exp. Therm. Fluid Sci. 103, 66–77.
Park, H.J., Tasaka, Y., Murai, Y., Oishi, Y., 2014. Vortical structures swept by a bubble swarm in turbulent boundary layers. Chem. Eng. Sci. 116, 486–496.
Ravelet, F., Colin, F., Risso, F., 2011. On the dynamics and breakup of a bubble rising in a turbulent flow. Phys. Fluids 23, 103301.
Rosti, M.E., Ge, Z., Jain, S.S., Dodd, M.S., Brandt, L., 2021. Droplets in homogeneous shear turbulence. J. Fluid Mech. 962–984, A109.
Sanders, W.C., Winkel, E.S., Dowling, D.R., Perlin, M., Ceccio, S.L., 2006. Bubble friction drag reduction in a high-Reynolds-number flat-plate turbulent boundary layer. J. Fluid Mech. 552, 353–380.
Schlatter, P., Örlü, R., 2010. Assessment of direct numerical simulation data of turbulent boundary layers. J. Fluid Mech. 659, 116–126.
Silberschmidt, N., Tasker, D., Pappas, T., Johannesson, J., 2016. Silverstream system-air lubrication performance verification and design development. In: Conference of Shipping in Changing Climate, Newcastle, UK. pp. 10–11.
Spandan, V., Lohse, D., Verzicco, R., 2016. Deformation and orientation statistics of neutrally buoyant sub-Kolmogorov ellipsoidal droplets in turbulent taylor–couette flow. J. Fluid Mech. 809, 480–504.
Spandan, V., Verzicco, R., Lohse, D., 2017. Deformable ellipsoidal bubbles in taylor-couette flow with enhanced Euler-Lagrangian tracking. Phys. Rev. Fluids 2, 104304.
Spandan, V., Verzicco, R., Lohse, D., 2018. Physical mechanisms governing drag reduction in turbulent taylor–couette flow with finite-size deformable bubbles. J. Fluid Mech. 849, R3.
Tanaka, T., Oishi, Y., Park, H.J., Tasaka, Y., Murai, Y., Kawakita, C., 2022. Frictional drag reduction caused by bubble injection in a turbulent boundary layer beneath a 36-m-long flat-bottom model ship. Ocean Eng. 252, 111224.
Tanaka, T., Park, H.J., Tasaka, Y., Murai, Y., 2020. Spontaneous and artificial void wave propagation beneath a flat-bottom model ship. Ocean Eng. 214, 107850.
Tutkun, M., George, W.K., Delvivlle, J., Stanislas, M., Johansson, P.B.V., Foucaut, J.-M., Coudert, S., 2009. Two-point correlations in high Reynolds number flat plate turbulent boundary layers. J. Turbul. 10, 1–23.
van den Berg, T.H., Luther, S., Lathrop, D.P., Lohse, D., 2005. Drag reduction in bubbly taylor-couette turbulence. Phys. Rev. Lett. 94, 044501.
Verschoof, R.A., van der Veen, R.C.A., Sun, C., Lohse, D., 2016. Bubble drag reduction requires large bubbles. Phys. Rev. Lett. 117, 104502.
Winkel, E., Ceccio, S.L., Dowling, D., Perlin, M., 2004. Bubble-size distributions produced by wall injection of air into flowing freshwater, saltwater and surfactant solutions. Exp. Fluids 37, 802–810.
Yoon, D., Park, H.J., Tasaka, Y., Murai, Y., 2022a. Drag coefficient of bubbles sliding beneath a towed model ship with variable tilt angles. Int. J. Multiph. Flow 149, 103995.
Yoon, D., Park, H.J., Tasaka, Y., Murai, Y., 2022b. Lift coefficient of bubble sliding inside turbulent boundary layers in an inclinable channel flow. Int. J. Multiph. Flow 149, 053301.